CONDENSED MATTER PHYSICS

$TaRh_2B_2$ and $NbRh_2B_2$: Superconductors with a chiral noncentrosymmetric crystal structure

Elizabeth M. Carnicom,[1]* Weiwei Xie,[2] Tomasz Klimczuk,[3] Jingjing Lin,[4] Karolina Górnicka,[3] Zuzanna Sobczak,[3] Nai Phuan Ong,[4] Robert J. Cava[1]*

It is a fundamental truth in solid compounds that the physical properties follow the symmetry of the crystal structure. Nowhere is the effect of symmetry more pronounced than in the electronic and magnetic properties of materials—even the projection of the bulk crystal symmetry onto different crystal faces is known to have a substantial impact on the surface electronic states. The effect of bulk crystal symmetry on the properties of superconductors is widely appreciated, although its study presents substantial challenges. The effect of a lack of a center of symmetry in a crystal structure, for example, has long been understood to necessitate that the wave function of the collective electron state that gives rise to superconductivity has to be more complex than usual. However, few nonhypothetical materials, if any, have actually been proven to display exotic superconducting properties as a result. We introduce two new superconductors that in addition to having noncentrosymmetric crystal structures also have chiral crystal structures. Because the wave function of electrons in solids is particularly sensitive to the host material's symmetry, crystal structure chirality is expected to have a substantial effect on their superconducting wave functions. Our two experimentally obtained chiral noncentrosymmetric superconducting materials have transition temperatures to superconductivity that are easily experimentally accessible, and our basic property characterization suggests that their superconducting properties may be unusual. We propose that their study may allow for a more in-depth understanding of how chirality influences the properties of superconductors and devices that incorporate them.

INTRODUCTION

The discovery of superconductivity in $CePt_3Si$ (*1*, *2*) has sparked interest in superconductors with noncentrosymmetric crystal structures (*3*) and their anomalous character (*4*). By far, most superconductors reported to date have inversion symmetry, which many believe to be a favorable trait in a superconducting material. When a superconductor has an inversion center, it can be classified as having either spin singlet or spin triplet pairing because the resulting spin degeneracy is protected by the inversion (*5*, *6*). However, for noncentrosymmetric crystal structures, conventional Cooper pairs can no longer form because the lack of inversion symmetry causes the Fermi surface to split (*7*). This splitting allows for mixed-parity pairing, which can result in complicated spin structures. The pairing can no longer be simply classified into even and odd parity, or as spin singlet or spin triplet (*8*). Such an admixture of spin states results in quasi-particle band structures (BSs) that are topologically nontrivial, which in turn results in a material with protected zero-energy states at the surface or edges, similar to topological insulators (*9*).

The violation of parity conservation can lead to various other exotic behaviors, such as magnetoelectric coupling (*10*) or anomalous upper critical field (μ_0H_{c2}) values, but does not guarantee such odd behavior (*3*). Some noncentrosymmetric superconductors have upper critical fields that exceed the Pauli limit ($\mu_0H^{Pauli} = 1.85*T_c$) (*11*, *12*), a limit that is based on the maximum magnetic field that will not break apart a singlet Cooper pair at low temperatures (*13*). The previously reported noncentrosymmetric superconductors such as $Mg_{10}Ir_{19}B_{16}$ (*14*, *15*), $Nb_{0.18}Re_{0.82}$ (*16*), T_2Ga_9 (T = Rh, Ir) (*17*), Li_2T_3B (T = Pd, Pt) (*18*, *19*), or other nonmagnetic analogs (*20*, *21*) of $CePt_3Si$, such as $LaPt_3Si$ (*22*), fit into categories based on whether they are both chiral and noncentrosymmetric or only noncentrosymmetric. Chiral crystal structures must also be noncentrosymmetric, but noncentrosymmetric crystal structures are not necessarily chiral. Although $Mg_{10}Ir_{19}B_{16}$ (*14*, *15*), $CePt_3Si$ (*1*, *2*), and $Nb_{0.18}Re_{0.82}$ (*16*) are noncentrosymmetric, their crystal structures are nonchiral, that is, they are non-enantiomorphic, but of these, only $CePt_3Si$ (*1*, *2*) displays a higher than expected H_{c2} value. On the other hand, Li_2T_3B (T = Pd, Pt) (*18*, *19*) and Mo_3Al_2C (*23*) are both noncentrosymmetric and have chiral crystal structures, but these materials display upper critical fields below the Pauli limit. In addition, researchers did not note or explore the potential effect of their structural chirality on superconductivity. Sr_2RuO_4 (*24*, *25*) and UPt_3 (*26*), which are both centrosymmetric and therefore structurally achiral, are, nonetheless, two of the main candidates believed to display chiral superconductivity (*27*). For a superconductor to be chiral, the phase of the superconducting gap function, $\Delta(\boldsymbol{k})$, must wind in either a counterclockwise or a clockwise direction as $\boldsymbol{k}$ moves along the Fermi surface (*27*). Adopting a chiral structure type does not necessarily result in chiral superconductivity, but Li_2Pt_3B, which has a chiral crystal structure, has also been proposed (*18*) as a candidate for chiral superconductivity.

Here, we report our discovery and investigation of the superconductors $TaRh_2B_2$ and $NbRh_2B_2$, which have a chiral noncentrosymmetric crystal structure, reporting their characterization through single-crystal x-ray diffraction, temperature-dependent electrical resistivity, magnetic susceptibility, and specific-heat measurements. They are isostructural, both forming in the same chiral noncentrosymmetric space group $P3_1$ (no. 144). We show that many of their properties are consistent with normal conventional superconducting behavior, but we also find that both $TaRh_2B_2$ and $NbRh_2B_2$ display anomalous upper critical field [$\mu_0H_{c2}(0)$] values that exceed the Pauli limit. We cannot rule out exotic pairing symmetries in the superconducting state for these materials.

[1]Department of Chemistry, Princeton University, Princeton, NJ 08544, USA. [2]Department of Chemistry, Louisiana State University, Baton Rouge, LA 70803, USA. [3]Department of Physics, Gdansk University of Technology, 80-233 Gdansk, Poland. [4]Department of Physics, Princeton University, Princeton, NJ 08544, USA.
*Corresponding author. Email: carnicom@princeton.edu (E.M.C.); rcava@exchange.princeton.edu (R.J.C.)

RESULTS AND DISCUSSION

Chiral crystal structure

We used single-crystal diffraction to determine the crystal structure of the new superconductor $TaRh_2B_2$, which crystallizes in the chiral, noncentrosymmetric space group $P3_1$ (no. 144), where $a = 4.6980(7)$ Å and $c = 8.770(2)$ Å. The space group and lattice parameters from the single-crystal refinement were the starting point for the LeBail fits of the room temperature powder x-ray diffraction (pXRD) patterns in Fig. 1A for $TaRh_2B_2$ (top) and isostructural $NbRh_2B_2$ (bottom). Note that Schaak *et al.* (*28*) anticipated the potential existence of superconductivity in a material of nominal composition $NbRh_2B_{2-y}$ with an unknown crystal structure. Only standard solid-state synthesis methods resulted in making the nearly single-phase bulk samples whose powder patterns are shown in Fig. 1A. Table S1 gives summary of the single-crystal structure refinement for $TaRh_2B_2$, and table S2 gives selected interatomic bond distances. Table 1 shows atomic coordinates from the crystal structure refinement. The 3_1 screw axis in the structure, which results in its chirality and also its lack of inversion symmetry, can be seen in Fig. 1B (top) when the structure is viewed along the *a* direction. The Ta, Rh spiral turns in either a right-handed or a left-handed direction within a superconducting domain, with B-B dimers interwoven throughout the spiral. Similar to other metal-rich boride superconductors such as NbRuB (*29*), which has isolated boron atoms in addition to B-B dimers, the B-B dimers in $TaRh_2B_2$ are also critical for stabilizing the compound. B-B dimers are not rare in borides—W_2CoB_2 (*30*), for example, also has B-B dimers in its structure. A better understanding of the crystal structure of $TaRh_2B_2$ results by viewing the structure along the *c* direction (Fig. 1B, bottom). The Ta atoms form isolated spirals (chains all turning in the same direction) that are surrounded by B-B dimers. The Ta spirals go through layers of Rh atoms arranged in a honeycomb lattice, where each honeycomb layer is slightly offset from the layer above and below, thus creating a spiral of Rh layers. The topology of the structure may host unique vortex states for the observed superconductivity. It may further help to understand the crystal structure to envision the Ta spirals as rods (*31*) penetrating the honeycomb layers of Rh that are themselves stacked in a spiral fashion. The B-B dimers stabilize the unusual structure through bonding to the metals.

Magnetic susceptibility

To characterize the superconductors $TaRh_2B_2$ and $NbRh_2B_2$, the field-dependent volume magnetization (M_V) was measured at 1.7 K (in the superconducting state) for both $TaRh_2B_2$ (Fig. 2A, inset) and $NbRh_2B_2$ (Fig. 2B, inset) and fitted to a line in the low-field region ($M_{fit} = bH + a$). The fit lines M_{fit} were used to estimate the demagnetization factor *N* (which is based on the sample shape and orientation with respect to the applied magnetic field) for both materials with the equation $-b = \frac{1}{4\pi(1-N)}$, using the slope of the fitted line, *b*. These *N* values were used to correct the magnetic susceptibility data in the main panels of Fig. 2 (A and B). We carried out further characterization through both zero-field–cooled (ZFC) and field-cooled (FC) temperature-dependent

Table 1. Atomic coordinates and equivalent isotropic displacement parameters of $TaRh_2B_2$ at 293(2) K. U_{eq} is defined as one-third of the trace of the orthogonalized U_{ij} tensor (Å^2).

Atom	Wyckoff position	Occupancy	*x*	*y*	*z*	U_{eq}
Ta	3*a*	1	0.8481(2)	0.8481(2)	0.3131(2)	0.0041(2)
Rh1	3*a*	1	0.6638(4)	0.4824(4)	0.0447(3)	0.0058(2)
Rh2	3*a*	1	0.3324(4)	0.8190(4)	0.1072(2)	0.0058(3)
B1	3*a*	1	0.627(7)	0.550(8)	0.549(3)	0.012(5)
B2	3*a*	1	0.288(9)	0.347(8)	0.215(3)	0.028(5)

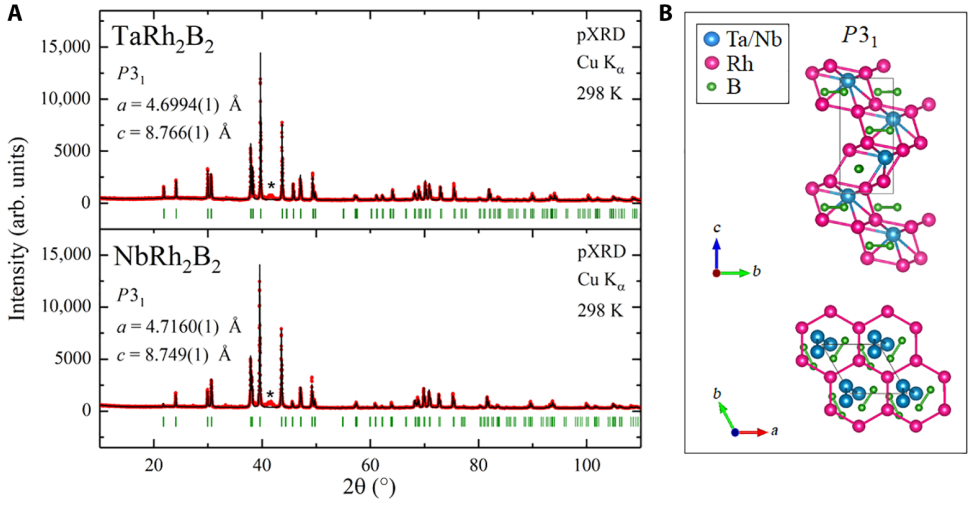

Fig. 1. Crystal structure characterization of $TaRh_2B_2$ and $NbRh_2B_2$. (**A**) Room temperature pXRD pattern showing a LeBail fit for the new superconducting phases $TaRh_2B_2$ (top) and $NbRh_2B_2$ (bottom). The experimentally observed data are shown with red circles, the calculated pattern is shown with a black line, and the green vertical marks indicate the expected Bragg reflections for space group $P3_1$ (no. 144). Impurity peaks are marked with asterisks. (**B**) The crystal structure of chiral and noncentrosymmetric $TaRh_2B_2$ and isostructural $NbRh_2B_2$ viewed along the *a* direction, emphasizing the 3_1 screw axis (top) and along the *c* direction (bottom), emphasizing the Ta spirals and a single Rh honeycomb layer. Tantalum/niobium is shown in blue, rhodium is shown in pink, and boron is shown in green. arb. units, arbitrary units.

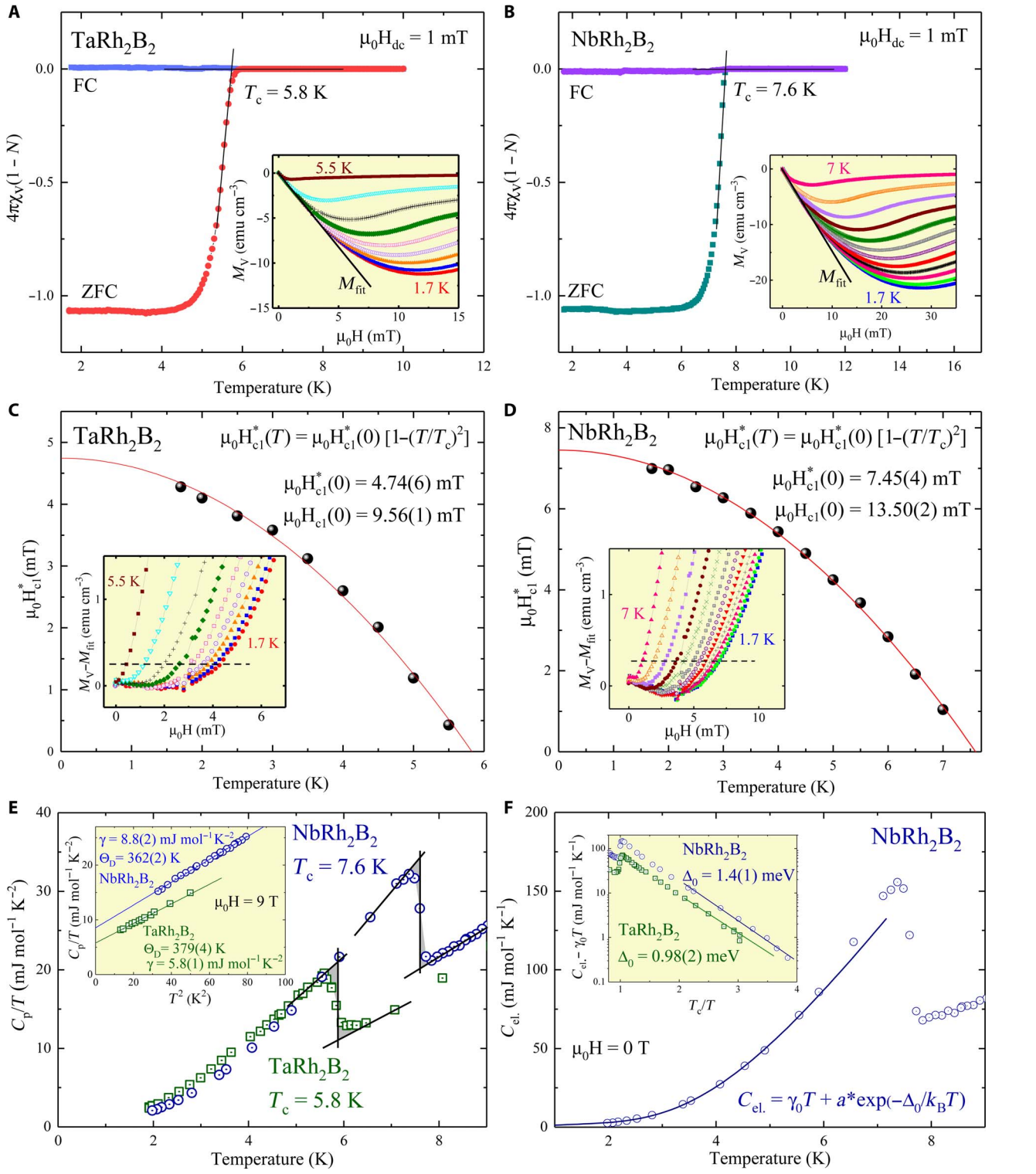

Fig. 2. Superconducting characterization of $TaRh_2B_2$ and $NbRh_2B_2$. (**A** and **B**) ZFC and FC temperature-dependent magnetic susceptibility $\chi_v(T)$ for $TaRh_2B_2$ (A) and $NbRh_2B_2$ (B) measured in an applied magnetic field of 1 mT. The insets show field-dependent volume magnetization (M_V) measured at various temperatures below T_c. (**C** and **D**) Lower critical field $\mu_0H^*_{c1}$ versus temperature for $TaRh_2B_2$ (A) and $NbRh_2B_2$ (B). The data points were estimated from a difference between M_V and M_{fit} as is shown in the insets. (**E**) C_p/T versus T plotted from 0 to 9 K for $TaRh_2B_2$ (green open squares) and $NbRh_2B_2$ (blue open circles) measured in zero applied field where the solid black lines outline the equal area construction shown with gray shading. This construction is used for estimation of T_c and the superconducting jump $\Delta C/T_c$. Inset: C_p/T versus T^2 measured in 9-T field (in the normal state) fitted to $C_p/T = \gamma + \beta T^2$. (**F**) Temperature-dependent electronic specific heat $C_{el.}$ for $NbRh_2B_2$ below 9 K. The solid curve through the data is a fit by a one-gap BCS model for superconductivity. Inset: $C_{el.} - \gamma_0 T$ versus normalized temperature (T_c/T) for $NbRh_2B_2$ and $TaRh_2B_2$. (The lattice contribution was subtracted from the measured specific heat). emu, electromagnetic unit.

magnetic susceptibility measurements with a 1-mT applied field. We took the measurement from 1.7 to 10 K for $TaRh_2B_2$ (Fig. 2A, main panel), showing a superconducting critical temperature of 5.8(1) K. We determined the T_c to be the intersection between the normal state of the magnetic susceptibility extrapolated to lower temperature with the line corresponding to the steepest slope of the diamagnetic signal (indicated by black solid lines) (*32*). We also performed ZFC and FC measurements on the Nb variant (Fig. 2B, main panel) from 1.7 K to 12 K, showing a T_c = 7.6(1) K. Both the ZFC and FC measurements were corrected for N = 0.504 for the Ta variant and N = 0.448 for the Nb variant. The resulting diamagnetic signal is only slightly less than the ideal value of $4\pi\chi_v(1 - N) = -1$ for both $TaRh_2B_2$ and $NbRh_2B_2$. The observed critical temperatures in the susceptibility measurements are consistent with both the specific heat and resistivity measurements (discussed next) for each superconducting material. There is a very weak superconducting signal observed for the FC measurement for each material, as expected due to the polycrystalline nature of both samples.

Magnetization

The new superconductors $TaRh_2B_2$ and $NbRh_2B_2$ were further studied with field-dependent magnetization (M_V) measurements at different temperatures below the critical temperature, as seen in Fig. 2A (inset) for the Ta variant and in Fig. 2B (inset) for the Nb variant. The low-field linear fits to the magnetization data (M_{fit}), as discussed previously, were used to construct the $M_V - M_{fit}$ plot in Fig. 2C (inset) for $TaRh_2B_2$ and $NbRh_2B_2$ (Fig. 2D, inset). The field at which the magnetization begins to deviate from a linear response (indicated by the black dashed line in each inset) is the uncorrected lower critical field, $\mu_0 H^*_{c1}$, for that temperature. All the $\mu_0 H^*_{c1}$ values with the corresponding temperatures are plotted in Fig. 2C (main panel) for $TaRh_2B_2$ and in Fig. 2D (main panel) for $NbRh_2B_2$ and fitted to the following equation

$$\mu_0 H^*_{c1}(T) = \mu_0 H^*_{c1}(0)\left[1 - \left(\frac{T}{T_c}\right)^2\right]$$

where $\mu_0 H^*_{c1}(0)$ is the lower critical field at 0 K and T_c is the superconducting critical temperature. $\mu_0 H^*_{c1}(0)$ was calculated to be 4.74(6) mT for $TaRh_2B_2$ and 7.45(4) mT for $NbRh_2B_2$. After correcting for the demagnetization factor for each sample, $\mu_0 H_{c1}(0)$ was calculated to be 9.56(1) mT for the Ta variant and 13.50(2) mT for the Nb variant.

Specific heat and observed superconducting parameters

The temperature-dependence of C_p/T is plotted for both $TaRh_2B_2$ and $NbRh_2B_2$ in Fig. 2E (main panel) under zero applied magnetic field measured from 2 to 9 K, showing a large anomaly in the specific heat for each superconducting material. Using equal-entropy constructions of the idealized specific heat capacity jump (gray shading), the T_c was determined to be 5.8 K for the Ta variant and 7.6 K for the Nb variant, consistent with the magnetic susceptibility and resistivity data.

At low temperature, the specific heat data can be described by the equation

$$\frac{C_p}{T} = \gamma + \beta T^2$$

where γT is the electronic contribution and βT^3 is the phonon contribution to the specific heat. This linear relationship can be seen in the C_p/T versus T^2 plot in the inset of Fig. 2E for $TaRh_2B_2$ and $NbRh_2B_2$. By fitting our data to the above equation (using data from the 9-T measurement taken from the normal state), the Sommerfeld parameter γ was calculated to be 5.8(1) mJ mol^{-1} K^{-2} for the Ta analog and 8.8(2) mJ mol^{-1} K^{-2} for the Nb analog. On the basis of the slope of each fitted line, β was calculated to be 0.178(5) mJ mol^{-1} K^{-4} for $TaRh_2B_2$ and β = 0.203(3) mJ mol^{-1} K^{-4} for $NbRh_2B_2$. The Debye model was then used with the β value in the equation

$$\Theta_D = \left(\frac{12\pi^4}{5\beta} nR\right)^{1/3}$$

to calculate the Debye temperature Θ_D, where n = 5 ($TaRh_2B_2$ or $NbRh_2B_2$) and R is the gas constant 8.314 J mol^{-1} K^{-1}. The Debye temperatures were calculated to be Θ_D = 379(4) K and Θ_D = 362(2) K for the Ta and Nb variants, respectively. With Θ_D and T_c, the electron-phonon coupling constant λ_{ep} can then be calculated using the inverted McMillan (*33*) equation

$$\lambda_{ep} = \frac{1.04 + \mu^* \ln\left(\frac{\Theta_D}{1.45T_c}\right)}{(1 - 0.62\mu^*)\ln\left(\frac{\Theta_D}{1.45T_c}\right) - 1.04}$$

where μ* = 0.13 and T_c = 5.8 and 7.6 K, respectively. The superconducting parameter λ_{ep} = 0.624(5) and 0.688(4) for $TaRh_2B_2$ and $NbRh_2B_2$, suggesting that both materials are weak-moderate coupling superconductors. Using λ_{ep}, γ, and the Boltzmann constant k_B, the density of electronic states at the Fermi energy $N(E_F)$ can be calculated from the equation

$$N(E_F) = \frac{3\gamma}{\pi^2 k_B^2 (1 + \lambda_{ep})}$$

$N(E_F)$ was estimated to be 1.52(3) states eV^{-1} per formula unit (fu) of $TaRh_2B_2$ and 2.21(5) states eV^{-1} per fu of $NbRh_2B_2$, respectively. In addition, the normalized specific heat jump, $\Delta C/\gamma T_c$, was found to be 1.56(4) and 1.60(3) for the Ta and Nb analogs, both of which are larger than the expected value of 1.43 (*34*), which suggests that both materials are moderately coupled superconductors.

Figure 2F (main panel) shows low-temperature (superconducting state) electronic specific heat $C_{el.}$ versus T for $NbRh_2B_2$ in zero applied field and fitted to the equation

$$C_{el.} = \gamma_0 T + a^* e^{-\frac{\Delta_0}{k_B T}}$$

where k_B is the Boltzmann constant, $\gamma_0 T$ is the electronic contribution to the specific heat coming from the sample impurities, and Δ_0 is the magnitude of the superconducting gap. $C_{el.} - \gamma_0 T$ plotted as a function of the normalized T_c/T for both $TaRh_2B_2$ and $NbRh_2B_2$ is shown in the inset of Fig. 2F. For a weak coupling superconductor (*34*)

$$2\Delta_0 = 3.5 k_B T_c$$

For $TaRh_2B_2$, the obtained value Δ_0 = 0.98(2) meV (for which $2\Delta_0$ = 1.96 meV) is larger than the theoretical value of $2\Delta_0$ = 1.75 meV (for T_c = 5.8 K). Likewise for $NbRh_2B_2$, the calculated value of Δ_0 = 1.4 (1)meV ($2\Delta_0$ = 2.8 meV) is larger than the expected value of $2\Delta_0$ = 2.29 meV (for

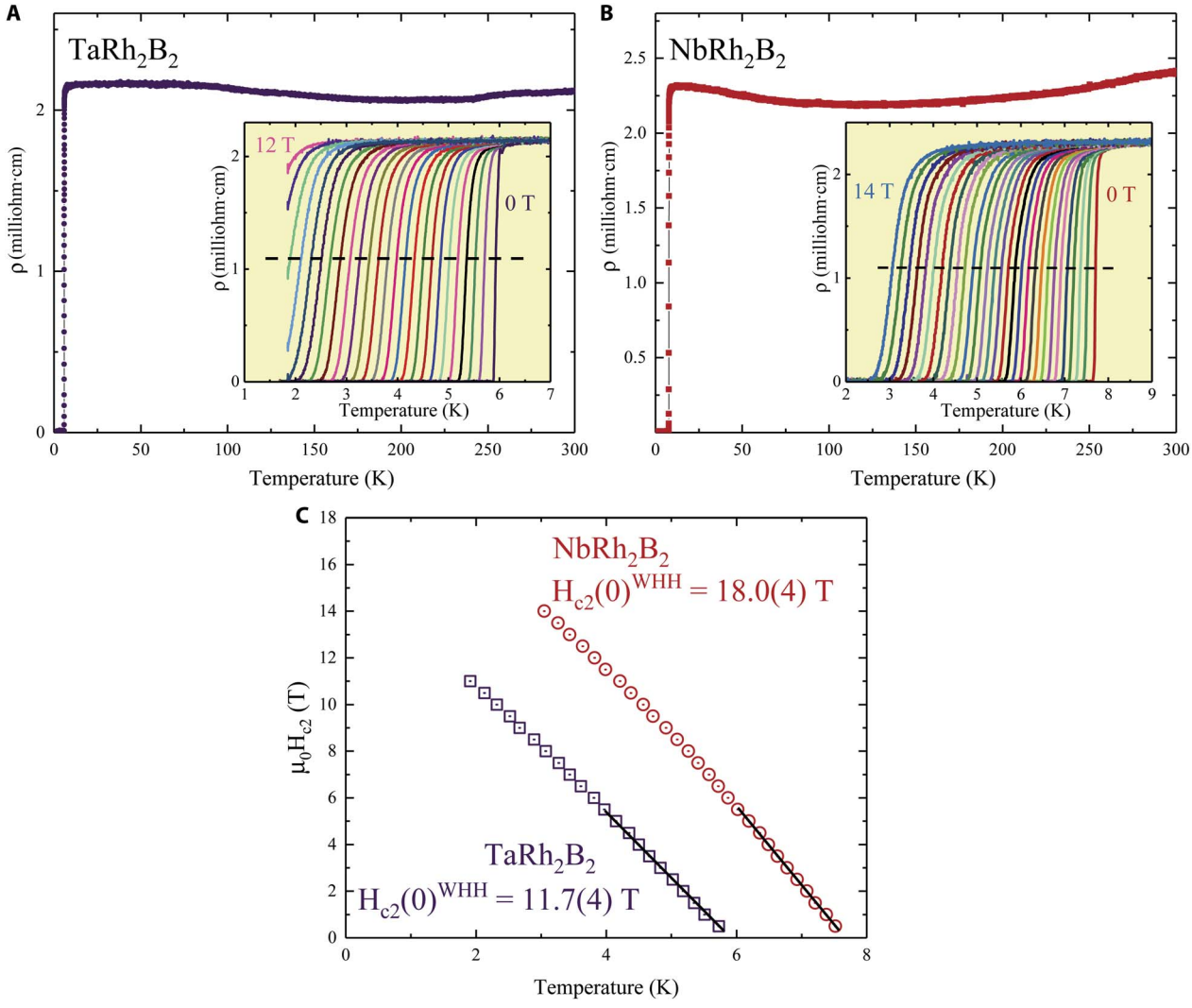

Fig. 3. Estimation of $\mu_0H_{c2}(0)$ from resistivity data. Temperature-dependent electrical resistivity for polycrystalline (**A**) $TaRh_2B_2$ and polycrystalline (**B**) $NbRh_2B_2$ measured from 300 to 1.7 K with zero applied magnetic field. Inset: Plot of the dependence of the superconducting transition on applied magnetic field measured (A) from 1.7 to 7 K for the Ta variant in applied fields from 0 to 12 T and (B) from 1.7 to 9 K for the Nb variant in applied magnetic fields from 0 to 14 T in 0.5-T increments. The dashed black line shows 50% of the superconducting transition. (**C**) The T_c values at different applied fields were used to calculate $\mu_0H_{c2}(0)$ to be 11.7(4) T for $TaRh_2B_2$ and 18.0(4) T for $NbRh_2B_2$.

T_c = 7.6 K), which is consistent with what we proposed previously that $TaRh_2B_2$ and $NbRh_2B_2$ are moderately coupled superconductors.

Resistivity

The temperature-dependent electrical resistivity measured from 300 to 1.7 K for polycrystalline $TaRh_2B_2$ is shown in Fig. 3A (main panel) and for polycrystalline $NbRh_2B_2$ in Fig. 3B (main panel). The resistivity drops to zero at 5.8 K for the Ta variant and at 7.7 K for the Nb variant. These new materials are both poor metals, and the resistivity is essentially temperature-independent for the temperature range above T_c. The dependence of T_c, taken as 50% of the resistivity transition (black dashed line), on the applied magnetic field is shown in the inset of Fig. 3A for $TaRh_2B_2$ and Fig. 3B for $NbRh_2B_2$, where the field is increased from 0 to 12 T in 0.5-T increments for the Ta variant and from 0 to 14 T for the Nb variant. Even with an 11-T applied magnetic field, the critical temperature was only suppressed to ~1.9 K for the Ta variant and to ~3 K for the Nb variant in a 14-T applied magnetic field.

Figure 3C shows the upper critical fields μ_0H_{c2} plotted as a function of the estimated T_c values and fitted to a line close to T_c for $TaRh_2B_2$ and $NbRh_2B_2$. The resulting slope ($d\mu_0H_{c2}/dT$) is −2.91(4) T/K for $TaRh_2B_2$ and −3.42(3) T/K for $NbRh_2B_2$. The 0-K upper critical field $\mu_0H_{c2}(0)$ can then be estimated using the Werthamer-Helfand-Hohenberg (WHH) equation (*35*)

$$\mu_0H_{c2}(0) = -AT_c\frac{d\mu_0H_{c2}}{dT}\Big|_{T=T_c}$$

where A is 0.693 for the dirty limit (which will be discussed later). Using T_c = 5.8 K for the Ta analog and T_c = 7.6 K for the Nb analog, the dirty limit $\mu_0H_{c2}(0)$ values were calculated to be 11.7(4) and 18.0(4) T, respectively. Both of these are high and even exceed the Pauli limit ($\mu_0H^{Pauli} = 1.85*T_c$), where μ_0H^{Pauli} = 10.7(2) T for $TaRh_2B_2$ and μ_0H^{Pauli} = 14.1(2) T for $NbRh_2B_2$. Even with a 14-T applied magnetic field (which is essentially equal to the Pauli limit for $NbRh_2B_2$), the T_c was only suppressed to 3 K, confirming a $\mu_0H_{c2}(0)$ value that exceeds the Pauli

limit. Likewise, for $TaRh_2B_2$, the last measurable T_c value was 1.9 K at 11 T, which is already above the Pauli limit for this material. A higher than expected $\mu_0H_{c2}(0)$ value has also been seen in the noncentrosymmetric superconductor $CePt_3Si$ (*1*, *2*), as discussed previously, which suggests that the superconductors reported here are potentially anomalous. In addition, it would be of future interest to perform measurements with the magnetic field applied along each axis direction of a single crystal to see whether the H_{c2} value displays anisotropy for each superconducting material.

The determined $\mu_0H_{c2}(0)$ and $\mu_0H_{c1}(0)$ values can be used to calculate several other superconducting parameters. Using the equation

$$\mu_0 H_{c2}(0) = \frac{\Phi_0}{2\pi\xi_{GL}^2}$$

where Φ_0 is the quantum flux h/2e, the Ginzburg-Landau coherence length ξ_{GL} was calculated to be 53(1) Å for $TaRh_2B_2$ and 43(1) Å for $NbRh_2B_2$. We used the dirty limit (discussed previously) to determine $\mu_0H_{c2}(0)$ because the obtained ratio of the coherence length ξ_{GL} and the mean free path (l) is close to 1 and therefore on the boundary between the dirty and clean limits. We determined the mean free path using the following equation [derived in the study of Singh *et al.* (*36*)]

$$l = 2.372 \times 10^{-14} \frac{\left(\frac{m^*}{m_e}\right)^2 V_M^2}{N(E_F)^2 \rho}$$

where V_M is the molar volume, ρ is the resistivity, and $N(E_F)$ is the density of states (DOS) at the Fermi level. For $TaRh_2B_2$, V_M = 33.6 cm^3 mol^{-1}, ρ = 2 milliohm·cm, $N(E_F)$ = 1.52(3) states eV^{-1} per fu, and assuming that $\frac{m^*}{m_e}$ = 1, we obtain l = 58 Å. Similarly, for $NbRh_2B_2$, V_M = 39.0 cm^3 mol^{-1}, ρ = 2.2 milliohm·cm, and $N(E_F)$ = 2.21(5) states eV^{-1} per fu, which gives l = 34 Å. The resulting ratios of ξ_{GL}/l are 0.9 and 1.3 for the Ta and Nb variants, respectively, which show that both $TaRh_2B_2$ and $NbRh_2B_2$ are on the border between the dirty limit and clean limit; we chose to use the dirty limit for the upper critical field calculations.

Using the result of ξ_{GL} with μ_0H_{c1} (determined previously), the superconducting penetration depth λ_{GL} = 2580(60) Å for the Ta analog and 2190(70) Å for the Nb analog were estimated using the lower critical field equation

$$\mu_0 H_{c1} = \frac{\Phi_0}{4\pi\lambda_{GL}^2} \ln\frac{\lambda_{GL}}{\xi_{GL}}$$

The value $\kappa_{GL} = \lambda_{GL}/\xi_{GL}$ was calculated to be κ_{GL} = 48(2) for $TaRh_2B_2$ and κ_{GL} = 51(3) for $NbRh_2B_2$, confirming the type II superconducting behavior in both new materials. Combining the results of H_{c1}, H_{c2}, and κ_{GL}, the thermodynamic critical field can be estimated from the equation

$$H_{c1}H_{c2} = H_c^2 \ln\kappa_{GL}$$

This calculation yields μ_0H_c = 169(3) mT for the Ta variant and 248(4) mT for the Nb variant. Table 2 gives a summary of all the observed superconducting parameters for $TaRh_2B_2$ and $NbRh_2B_2$, with a chiral noncentrosymmetric crystal structure.

Table 2. Observed superconductivity parameters of $TaRh_2B_2$ and $NbRh_2B_2$.

Parameter	Units	$TaRh_2B_2$	$NbRh_2B_2$
T_c	K	5.8(1)	7.6(1)
$\mu_0H_{c1}(0)$	mT	9.56(1)	13.50(2)
$\mu_0H_{c2}(0)$	T	11.7(4)	18.0(4)
$\mu_0H_c(0)$	mT	169(3)	248(4)
ξ_{GL}	Å	53(1)	43(1)
λ_{GL}	Å	2580(60)	2190(70)
κ_{GL}	—	48(2)	51(3)
γ	mJ mol^{-1} K^{-2}	5.8(1)	8.8(2)
$\Delta C/\gamma T_c$	—	1.56(4)	1.60(3)
μ_0H^{Pauli}	T	10.7(2)	14.1(2)
λ_{ep}	—	0.624(5)	0.688(4)
$N(E_F)$	states eV^{-1} per fu	1.52(3)	2.21(5)
Θ_D	K	379(4)	362(2)
Δ_0	meV	0.98(2)	1.4(1)

Electronic structure

To gain an intrinsic insight into the relationship between the superconductivity observed and the electronic states of $TaRh_2B_2$ and $NbRh_2B_2$, we investigated the electronic DOS and BS for both superconducting materials without and with spin-orbit coupling (SOC) (Fig. 4). The total and partial DOS for $TaRh_2B_2$ and $NbRh_2B_2$ are illustrated in Fig. 4 (C and F). The DOS in the energy below −2.0 eV mainly consists of Ta/Nb and Rh *s* and *d* orbitals. The DOS in the energy range from −2.0 to +2.0 eV contains mixed Ta/Nb and Rh *s* and *d* orbitals in addition to *s* and *p* orbitals from B, in particular, around the Fermi level. Note that the calculated DOS(E_F) values are 1.3 states eV^{-1} per fu of $TaRh_2B_2$ and 1.5 states eV^{-1} per fu of $NbRh_2B_2$; these obey the same qualitative behavior as the observed values presented in Table 2. A sharp peak in the DOS is often an indication of a nearby structural, electronic, or magnetic instability such as superconductivity. To investigate further, we calculated the BS both with/without SOC for $TaRh_2B_2$ (Fig. 4, A and B) and for $NbRh_2B_2$ (Fig. 4, D and E). The broad peak in the DOS at E_F is due to the presence of saddle points in the electronic structure at the M and L points in the Brillouin zone. Researchers have often proposed that Saddle points near E_F are important for yielding superconductivity (*37*) and they may also be significant in the current materials.

In summary, we report two new noncentrosymmetric superconductors, $TaRh_2B_2$ and $NbRh_2B_2$, which both have a new crystal structure belonging to the chiral space group $P3_1$. Temperature-dependent electrical resistivity, magnetic susceptibility, and specific heat data confirmed bulk superconductivity with T_c = 5.8 K for the Ta analog and T_c = 7.6 K for the Nb analog. The derived superconducting parameters show that $TaRh_2B_2$ and $NbRh_2B_2$ are basically type II Bardeen, Cooper, Schrieffer (BCS) moderately coupled superconductors. However, their

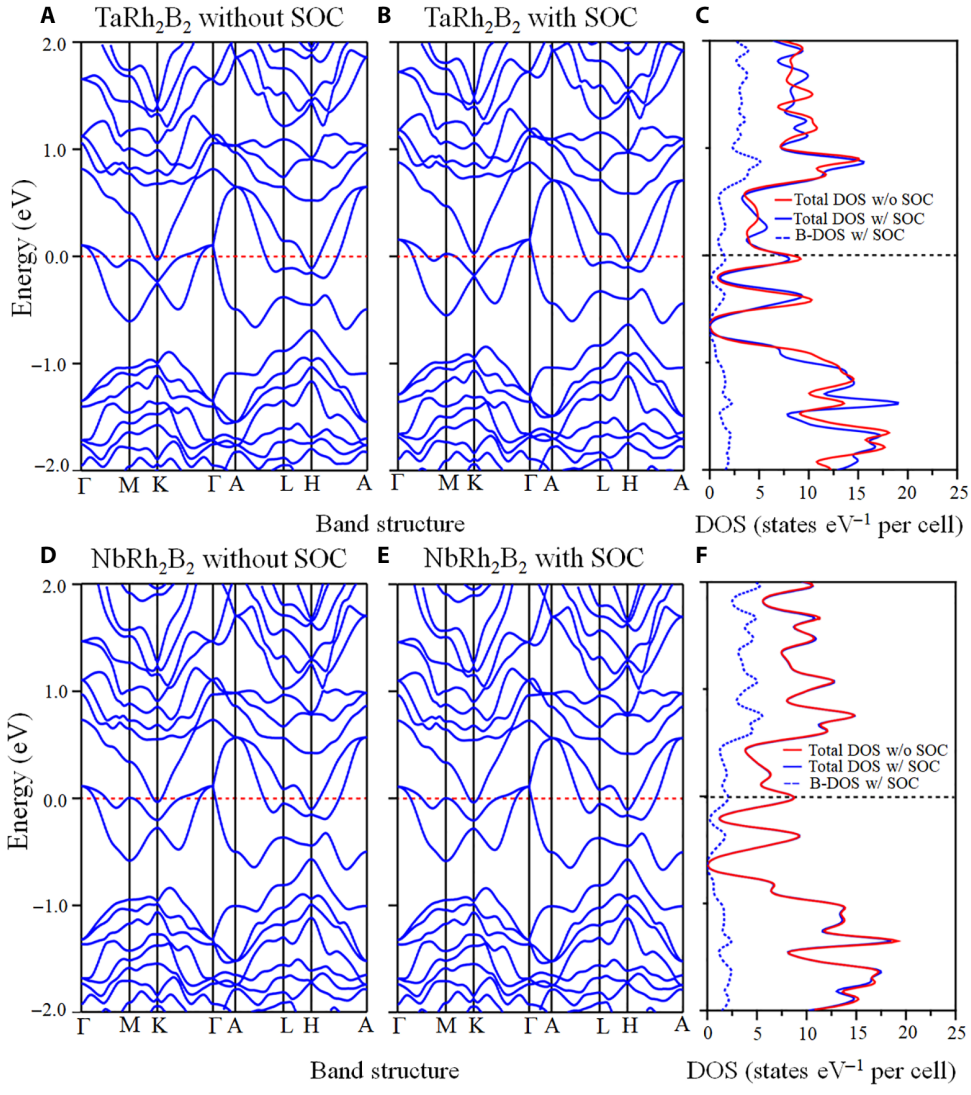

Fig. 4. Electronic calculations for $TaRh_2B_2$ and $NbRh_2B_2$. Calculated BS for (**A** and **B**) $TaRh_2B_2$ and (**D** and **E**) $NbRh_2B_2$ both with (middle) and without (left) SOC plotted in the energy range from −2.0 to 2.0 eV. The total DOS calculated using the Wien2K with LDA-type pseudopotentials with SOC included (blue line) and without SOC (red line) for (**C**) $TaRh_2B_2$ and (**F**) $NbRh_2B_2$.

behavior under applied magnetic fields shows that $\mu_0 H_{c2}(0)$ exceeds the Pauli limit for both superconducting materials. Although many of the superconducting properties are conventional, we cannot rule out more complicated spin states in the superconducting state. Future work on these materials to determine whether their chiral noncentrosymmetric crystal structure has an effect on their normal state and superconducting properties, and on their use in advanced devices, particularly those with chirality junctions, will be of interest.

MATERIALS AND METHODS

Experimental design

The starting materials for the synthesis of $TaRh_2B_2$ and $NbRh_2B_2$ bulk materials were elemental tantalum (>99.9%, 100 mesh; Alfa), niobium (>99.9%, 200 mesh; Sigma-Aldrich), rhodium (>99.9%, 325 mesh; Alfa), and boron (submicron particles, Callery Chemical). Powders of the starting materials Ta/Nb, Rh, and B were weighed out in a 1:1.9:2.1 ratio, ground using a mortar and pestle, and pressed into a pellet. The samples were then wrapped in Ta foil, placed in an alumina crucible, and heated in a high vacuum furnace to 1200°C for 6 hours. Variation from the above loading compositions or heating temperature led to the presence of secondary phases in larger amounts. Attempts to arc-melt $TaRh_2B_2$ followed by annealing at 1100°C for 1 week in an evacuated silica tube did not result in a single-phase sample. Samples of $TaRh_2B_2$ and $NbRh_2B_2$ are stable in air and do not decompose over time.

Crystal structure characterization

The purity of the samples studied was checked using room temperature pXRD using a Bruker D8 Advance Eco Cu K_α radiation (λ = 1.5406 Å) diffractometer with a LynxEye-XE detector. Single crystals from an arc-melted and annealed sample of $TaRh_2B_2$ were mounted on the tips of Kapton loops. A Bruker Apex II x-ray diffractometer with Mo $K_{\alpha 1}$ radiation (λ = 0.71073 Å) was used to collect room temperature intensity data. The data were collected over a full sphere of reciprocal space with

0.5° scans in ω, 10 s per frame of exposure time, and a 2θ range from 4° to 75°. The SMART software was used to acquire all data, and the SAINT program was used to both extract intensities and to correct for polarization and Lorentz effects. XPREP was used to perform numerical absorption corrections (*38*). Twinning of the unit cell was tested. The crystal structure of $TaRh_2B_2$ was solved using direct methods and refined by full-matrix least-squares on F^2 with the SHELXTL package (*39*). A total of 25 space groups were tested according to the observed Laue symmetry, and the space group was determined to be $P3_1$. To the best of our knowledge, $TaRh_2B_2$ has a unique structure type. The crystal structure images were created in the program VESTA (*40*). Because boron is such a light element and therefore difficult to quantify using x-ray diffraction, the B content determined in the refinement was tested further through synthesis of materials of different boron contents. These syntheses resulted in significant amounts of impurity phases. Finally, the surfaces of the Ta-Rh-B samples were analyzed for their Ta and Rh content using an FEI Quanta 250FEG scanning electron microscope equipped with an Apollo-X SDD energy-dispersive spectrometer (EDS). EDAX TEAM software was used to process the EDS data by using standardless quantitative analysis. The EDS data confirmed a Ta/Rh ratio of 1:2, consistent with the results from the single-crystal refinement. The FullProf Suite program was used to perform LeBail refinements on bulk samples of both $TaRh_2B_2$ and $NbRh_2B_2$ using Thompson-Cox-Hastings pseudo-Voigt peak shapes. Lattice parameters determined from single-crystal data were consistent with those determined from the LeBail fit for $TaRh_2B_2$. The same structure with slightly different cell parameters was also found to index the diffraction pattern for $NbRh_2B_2$.

Superconducting property measurements

A Quantum Design Physical Property Measurement System (PPMS) Dynacool was used to measure the temperature- and field-dependent magnetization and temperature-dependent electrical resistivity of $TaRh_2B_2$ and $NbRh_2B_2$ using a vibrating sample magnetometer and resistivity option. Both ZFC and FC magnetic susceptibility measurements were taken from 1.7 to 10 K for the Ta variant and from 1.7 K to 12 K for the Nb variant with a 1-mT applied magnetic field. The field-dependent magnetization was measured at various temperatures for both $TaRh_2B_2$ and $NbRh_2B_2$ for fields in the range 0 to 15.0 mT for the Ta variant and 0 to 35.0 mT for the Nb variant. The temperature-dependent electrical resistivity measurements were carried out using a standard four-probe method from 300 to 1.7 K with an applied current of 2 mA and zero applied magnetic field. The resistivity was then measured in the low-temperature region from 1.7 to 7 K for the Ta variant and 1.7 K to 9 K for the Nb variant with applied magnetic fields varying from 0 to 9 T in 0.5-T increments. A 14-T Quantum Design PPMS was used to measure the high field temperature–dependent resistivity of both $NbRh_2B_2$ and $TaRh_2B_2$ with a 2-mA applied current in 0.5-T increments. Specific heat data for both $TaRh_2B_2$ and $NbRh_2B_2$ were collected on a Quantum Design PPMS Evercool II with applied magnetic fields of 0 and 9 T.

Electronic structure calculations

The BS and DOS of $TaRh_2B_2$ and $NbRh_2B_2$ were calculated using Wien2K with LDA-type (local density approximation) pseudopotentials. The structural lattice parameters obtained from single-crystal diffraction experiments for $TaRh_2B_2$ were used for the calculation. SOC was included for all atoms. Reciprocal space integrations were completed over an 8 × 8 × 4 Monkhorst-Pack *k*-points mesh. The convergence criterion for a self-consistent calculation was taken as 1.0×10^{-4} eV.

SUPPLEMENTARY MATERIALS

Supplementary material for this article is available at http://advances.sciencemag.org/cgi/content/full/4/5/eaar7969/DC1

table S1. Single-crystal crystallographic data for $TaRh_2B_2$.

table S2. Selected bond distances for $TaRh_2B_2$.

REFERENCES AND NOTES

1. E. Bauer, G. Hilscher, H. Michor, C. Paul, E. W. Scheidt, A. Gribanov, Y. Seropegin, H. Noël, M. Sigrist, P. Rogl, Heavy fermion superconductivity and magnetic order in noncentrosymmetric $CePt_3Si$. *Phys. Rev. Lett.* **92**, 027003 (2004).
2. K. V. Samokhin, E. S. Zijlstra, S. K. Bose, $CePt_3Si$: An unconventional superconductor without inversion center. *Phys. Rev. B* **69**, 094514 (2004).
3. S. Yip, Noncentrosymmetric superconductors. *Annu. Rev. Condens. Matter Phys.* **5**, 15–33 (2014).
4. I. Sugitani, Y. Okuda, H. Shishido, T. Yamada, A. Thamizhavel, E. Yamamoto, T. D. Matsuda, Y. Haga, T. Takeuchi, R. Settai, Y. Ōnuki, Pressure-induced heavy-fermion superconductivity in antiferromagnet $CeIrSi_3$ without inversion symmetry. *J. Phys. Soc. Jpn.* **75**, 043703 (2006).
5. S. Yip, A. Garg, Superconducting states of reduced symmetry: General order parameters and physical implications. *Phys. Rev. B* **48**, 3304–3308 (1993).
6. E. I. Blount, Symmetry properties of triplet superconductors. *Phys. Rev. B* **32**, 2935–2944 (1985).
7. R. P. Kaur, D. F. Agterberg, M. Sigrist, Helical vortex phase in the noncentrosymmetric $CePt_3Si$. *Phys. Rev. Lett.* **94**, 137002 (2005).
8. T. Grant, A. J. S. Machado, D. J. Kim, Z. Fisk, Superconductivity in non-centrosymmetric $ThCoC_2$. *Supercond. Sci. Technol.* **27**, 035004 (2014).
9. A. P. Schnyder, P. M. R. Brydon, C. Timm, Types of topological surface states in nodal noncentrosymmetric superconductors. *Phys. Rev. B* **85**, 024522 (2012).
10. V. M. Edelstein, Magnetoelectric effect in polar superconductors. *Phys. Rev. Lett.* **75**, 2004–2007 (1995).
11. V. P. Mineev, Paramagnetic limit of superconductivity in a crystal without an inversion center. *Phys. Rev. B* **71**, 012509 (2005).
12. N. Kimura, K. Ito, H. Aoki, S. Uji, T. Terashima, Extremely high upper critical magnetic field of the noncentrosymmetric heavy fermion superconductor $CeRhSi_3$. *Phys. Rev. Lett.* **98**, 197001 (2007).
13. A. M. Clogston, Upper limit for the critical field in hard superconductors. *Phys. Rev. Lett.* **9**, 266–267 (1962).
14. T. Klimczuk, Q. Xu, E. Morosan, J. D. Thompson, H. W. Zandbergen, R. J. Cava, Superconductivity in noncentrosymmetric $Mg_{10}Ir_{19}B_{16}$. *Phys. Rev. B* **74**, 220502(R) (2006).
15. T. Klimczuk, F. Ronning, V. Sidorov, R. J. Cava, J. D. Thompson, Physical properties of the noncentrosymmetric superconductor $Mg_{10}Ir_{19}B_{16}$. *Phys. Rev. Lett.* **99**, 257004 (2007).
16. A. B. Karki, Y. M. Xiong, N. Haldolaarachchige, S. Stadler, I. Vekhter, P. W. Adams, D. P. Young, W. A. Phelan, J. Y. Chan, Physical properties of the noncentrosymmetric superconductor $Nb_{0.18}Re_{0.82}$. *Phys. Rev. B* **83**, 144525 (2011).
17. T. Shibayama, M. Nohara, H. Aruga Katori, Y. Okamoto, Z. Hiroi, H. Takagi, Superconductivity in Rh_2Ga_9 and Ir_2Ga_9 without inversion symmetry. *J. Phys. Soc. Jpn.* **76**, 073708 (2007).
18. H. Q. Yuan, D. F. Agterberg, N. Hayashi, P. Badica, D. Vandervelde, K. Togano, M. Sigrist, M. B. Salamon, *S*-wave spin-triplet order in superconductors without inversion symmetry: Li_2Pd_3B and Li_2Pt_3B. *Phys. Rev. Lett.* **97**, 017006 (2006).
19. K. Togano, P. Badica, Y. Nakamori, S. Orimo, H. Takeya, K. Hirata, Superconductivity in the metal rich Li-Pd-B ternary boride. *Phys. Rev. Lett.* **93**, 247004 (2004).
20. E. Bauer, R. T. Khan, H. Michor, E. Royanian, A. Grytsiv, N. Melnychenko-Koblyuk, P. Rogl, D. Reith, R. Podloucky, E.-W. Scheidt, W. Wolf, M. Marsman, $BaPtSi_3$: A noncentrosymmetric BCS-like superconductor. *Phys. Rev. B* **80**, 064504 (2009).
21. M. Isobe, H. Yoshida, K. Kimoto, M. Arai, E. Takayama-Muromachi, $SrAuSi_3$: A noncentrosymmetric superconductor. *Chem. Mater.* **26**, 2155–2165 (2014).
22. I. Kawasaki, I. Watanabe, H. Amitsuka, K. Kunimori, H. Tanida, Y. Ōnuki, Superconducting properties of noncentrosymmetric superconductor $LaPt_3Si$ studied by muon spin spectroscopy. *J. Phys. Soc. Jpn.* **82**, 084713 (2013).
23. A. B. Karki, Y. M. Xiong, I. Vekhter, D. Browne, P. W. Adams, D. P. Young, K. R. Thomas, J. Y. Chan, H. Kim, R. Prozorov, Structure and physical properties of the noncentrosymmetric superconductor Mo_3Al_2C. *Phys. Rev. B* **82**, 064512 (2010).
24. Y. Maeno, H. Hashimoto, K. Yoshida, S. Nishizaki, T. Fujita, J. G. Bednorz, F. Lichtenberg, Superconductivity in a layered perovskite without copper. *Nature* **372**, 532–534 (1994).
25. Y. Maeno, S. Kittaka, T. Nomura, S. Yonezawa, K. Ishida, Evaluation of spin-triplet superconductivity in Sr_2RuO_4. *J. Phys. Soc. Jpn.* **81**, 011009 (2012).
26. J. A. Sauls, The order parameter for the superconducting phases of UPt_3. *Adv. Phys.* **43**, 113–141 (1994).
27. C. Kallin, J. Berlinsky, Chiral superconductors. *Rep. Prog. Phys.* **79**, 054502 (2016).
28. R. E. Schaak, M. Avdeev, W.-L. Lee, G. Lawes, H. W. Zandbergen, J. D. Jorgensen, N. P. Ong, A. P. Ramirez, R. J. Cava, Formation of transition metal boride and carbide perovskites related to superconducting $MgCNi_3$. *J. Solid State Chem.* **177**, 1244–1251 (2004).

29. W. Xie, H. Luo, K. Baroudi, J. W. Krizan, B. F. Phelan, R. J. Cava, Fragment-based design of NbRuB as a new metal-rich boride superconductor. *Chem. Mater.* **27**, 1149–1152 (2015).
30. W. Rieger, H. Nowotny, F. Benesovsky, Die Kristallstruktur von W_2CoB_2 und isotypen Phasen. *Monatshefte für Chemie* **97**, 378–382 (1966).
31. M. O'Keeffe, S. Andersson, Rod packings and crystal chemistry. *Acta Crystallogr.* **A33**, 914–923 (1977).
32. T. Klimczuk, R. J. Cava, Carbon isotope effect in superconducting $MgCNi_3$. *Phys. Rev. B* **70**, 212514 (2004).
33. W. L. McMillan, Transition temperature of strong-coupled superconductors. *Phys. Rev.* **167**, 331–344 (1968).
34. M. Tinkham, *Introduction to Superconductivity* (Dover Publications, Inc., Mineola, ed. 2, 1996).
35. N. R. Werthamer, E. Helfand, P. C. Hohenberg, Temperature and purity dependence of the superconducting critical field, H_{c2}. III. Electron Spin and spin-orbit effects. *Phys. Rev.* **147**, 295–302 (1966).
36. Y. Singh, C. Martin, S. L. Bud'ko, A. Ellern, R. Prozorov, D. C. Johnston, Multigap superconductivity and Shubnikov-de Haas oscillations in single crystals of the layered boride OsB_2. *Phys. Rev. B* **82**, 144532 (2010).
37. D. M. Newns, H. R. Krishnamurthy, P. C. Pattnaik, C. C. Tsuei, C. C. Chi, C. L. Kane, Van Hove scenario for cuprate superconductivity. *Physica B.* **186–188**, 801–807 (1993).
38. SHELXTL Software Reference Manual, Version 6.10 (Bruker Analytical X-Ray System, Inc., Madison, WI, 2000).
39. G. M. Sheldrick, A short history of *SHELX*. *Acta Crystallogr.* **A64**, 112–122 (2008).
40. K. Momma, F. Izumi, VESTA 3 for three-dimensional visualization of crystal, volumetric and morphology data. *J. Appl. Crystallogr.* **44**, 1272–1276 (2011).

Acknowledgments
Funding: The materials synthesis was supported by the U.S. Department of Energy, Division of Basic Energy Sciences (grant DE-FG02-98ER45706), and the property characterization was supported by the Gordon and Betty Moore Foundation EPiQS initiative (grant GBMF-4412). The work at Louisiana State University (LSU) was supported by the Board of Regents Research Competitiveness Subprogram under contract number LEQSF (2017-20)-RD-A-08 and LSU startup funding. The research in Poland was supported by the National Science Centre (grant UMO-2016/22/M/ST5/00435). N.P.O. acknowledges the support of the Gordon and Betty Moore Foundations EPiQS Initiative through grant GBMF4539. J.L. was supported by funds from the NSF, NSF MRSEC (Materials Research Science and Engineering Centers) grant DMR 1420541. **Author contributions:** E.M.C. synthesized the superconducting materials, measured the magnetic susceptibility, and wrote the draft of the manuscript. W.X. determined the crystal structure and carried out the electronic structure calculations. T.K. helped synthesize the materials, contributed to the data analysis, helped with drafts of figures, and supervised characterization measurements. K.G. measured the specific heat. Z.S. carried out both energy-dispersive x-ray analysis and specific heat measurements. J.L. measured the resistivity. N.P.O. supervised the high-field transport measurements. R.J.C. supervised the project and property measurements, helped analyze the experimental data, and revised the draft. All authors helped revise the manuscript. **Competing interests:** The authors declare that they have no competing interests. **Data and materials availability:** All data supporting the stated conclusions of the manuscript are in the paper or in the Supplementary Materials. The crystal structure cif file has been deposited in the Cambridge Crystallographic Data Centre. Additional data are available from the authors upon request.

Submitted 19 December 2017
Accepted 20 March 2018
Published 4 May 2018
10.1126/sciadv.aar7969

Citation: E. M. Carnicom, W. Xie, T. Klimczuk, J. Lin, K. Górnicka, Z. Sobczak, N. P. Ong, R. J. Cava, $TaRh_2B_2$ and $NbRh_2B_2$: Superconductors with a chiral noncentrosymmetric crystal structure. *Sci. Adv.* **4**, eaar7969 (2018).